THE JOURNAL OF
PHYSICAL CHEMISTRY C
Article
Cite This: J. Phys. Chem. C 2019, 123, 26695−26704
pubs.acs.org/JPCC

Photothermal Effect, Local Field Dependence, and Charge Carrier Relaying Species in Plasmon-Driven Photocatalysis: A Case Study of Aerobic Nitrothiophenol Coupling Reaction

Qingfeng Zhang,[†] Yadong Zhou,[‡] Xiaoqi Fu,[†,§] Esteban Villarreal,[†] Lichao Sun,[†] Shengli Zou,[‡] and Hui Wang*,[†]

[†]Department of Chemistry and Biochemistry, University of South Carolina, 631 Sumter Street, Columbia, South Carolina 29208, United States

[‡]Department of Chemistry, University of Central Florida, Orlando, Florida 32816, United States

[§]School of Chemistry and Chemical Engineering, Jiangsu University, Zhenjiang, Jiangsu 212013, China

Supporting Information

ABSTRACT: Optical excitation of plasmonic electron oscillations confined by metallic nanoparticles provides a unique means of driving unconventional photocatalytic transformations of molecular adsorbates on the nanoparticle surfaces. Photothermal heating, local-field enhancement, and hot carrier generation have been identified as three major plasmon-induced photophysical effects, all of which are directly relevant to plasmon-driven photocatalysis. However, delineation of the contribution of each effect has long been challenging due to the strong synergy among the three effects and the mechanistic complexity of plasmon-driven molecular transformations. Aiming at unambiguously elucidating the photothermal effect, local-field dependence, and hot carrier channeling mechanisms that underpin plasmon-driven photocatalysis, we conducted a detailed case study on the aerobic reductive coupling of *p*-nitrothiophenol chemisorbed on Ag nanocube surfaces under near-infrared excitations. We used surface-enhanced Raman scattering (SERS) as a plasmon-enhanced, molecular fingerprinting spectroscopic tool to track the plasmon-driven structural evolution of molecular adsorbates in real time, based on which we were able to correlate the molecule-transforming kinetics with local-field intensities and photothermal heating at the nanoparticle surfaces. The information extracted from the time-resolved SERS results allowed us not only to clarify several controversial issues regarding the photothermal effect and local field dependence but also to unravel a unique function of surface-adsorbed molecular oxygen as an interfacial charge carrier relaying cocatalyst that works in conjunction with the plasmonic Ag photocatalysts to mediate the multistep coupling reaction.

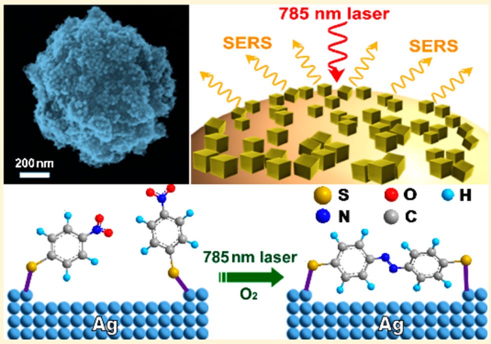

■ INTRODUCTION

Optically excited collective oscillations of conduction electrons in metallic nanoparticles, also known as localized plasmons, provide a unique means to activate unconventional photocatalytic reactions that are otherwise either thermodynamically nonspontaneous or kinetically sluggish under thermal conditions.[1−6] Plasmons may decay radiatively through photon scattering or nonradiatively through Landau damping.[1,2] Upon radiative plasmon decay, a metallic nanoparticle functions as a nanoscale light-concentrating antenna, creating electromagnetic "hot spots" on its surface with immensely enhanced local fields exploitable not only for plasmon-enhanced spectroscopies[7−10] but also for boosting catalytic transformations of molecular adsorbates.[11,12] Through the nonradiative Landau damping, a plasmon quantum is transferred into the excitation of an electron−hole pair, giving rise to transient, nonthermally distributed hot electrons, which can be injected into unpopulated orbitals of molecular adsorbates to trigger a series of intriguing bond-breaking and bond-forming processes.[1−6,13−19] A potentially more efficient charge transfer channel involves direct excitation of a plasmonic hot electron in a molecular adsorbate[2,20,21] or semiconductor that is strongly coupled with the metal nanoparticle.[22] The short-lived plasmonic hot carriers may also undergo a multistep decay process to become thermalized by redistributing their energies through electron−electron and electron−phonon interactions over multiple time scales ranging from subpicoseconds to nanoseconds.[1] The thermal relaxation of hot carriers leads to localized photothermal heating in the vicinity of the nanoparticle surfaces, effectively depositing thermal energy into the molecular adsorbates to accelerate the interfacial catalytic reactions.[23,24] While photothermal heating, local-field enhancement, and hot carrier generation have been identified as three major plasmonic effects all directly relevant

Received: August 27, 2019
Revised: September 29, 2019
Published: October 4, 2019

DOI: 10.1021/acs.jpcc.9b08181
J. Phys. Chem. C 2019, 123, 26695−26704

to plasmon-driven photocatalysis, it has long been a challenging task to delineate the contribution of each effect due to the strong interplay among them and the mechanistic complexity of plasmon-driven reactions.[25−27]

This work aims at shedding light on the photothermal effect, local-field dependence, and hot carrier transfer channels underpinning plasmon-driven photocatalysis through a detailed case study on the formation of 4,4′-dimercaptoazobenzene (DMAB) via reductive coupling of *p*-nitrothiophenol (*p*NTP). This reaction has been a prototypical plasmon-driven chemical transformation process ideal for detailed mechanistic investigations because its kinetics depends critically on the excitation wavelength, the excitation power density, the local reaction environments, and the plasmonic nanostructures on which the reactant molecules are adsorbed.[28−41] Although this reaction has been intensively investigated under a diverse set of reaction conditions, several key aspects regarding the detailed mechanisms are still under intense debate. (1) There are multiple pieces of experimental evidence coherently showing that this reaction is driven by hot electrons and can be kinetically boosted by photothermal heating.[34−37] However, no consensus has been reached regarding to what degree and through which mechanism the photothermal heating influences the reaction kinetics.[34−37] (2) In line with common-sense expectation, the reaction rate has been observed to increase with the local field intensities at the surface sites where the molecules are located.[38−40] As revealed by a recent study, however, the reaction kinetics appears independent of the local fields when the *p*NTP coupling reaction occurs on nanostructured Au surfaces under near-infrared excitations.[41] These counterintuitive results imply that the local-field dependence of this plasmon-driven reaction needs to be reexamined more carefully. (3) The first elementary step initiating the reductive *p*NTP coupling has been identified to be the hot electron transfer from the metallic photocatalysts to surface-adsorbed *p*NTP.[38] On Ag substrates, this hot electron transfer process requires an excitation energy above 1.7 eV (wavelength < ~720 nm) because the lowest unoccupied molecular orbital (LUMO) of surface-adsorbed *p*NTP lies ~1.7 eV above the Fermi level of Ag.[42] The threshold excitation energy for the Au-to-*p*NTP hot electron transfer is expected to be even higher because the Fermi level of Au is ~0.7 eV further below that of Ag.[42] Surprisingly, the reductive coupling of *p*NTP may still occur rapidly under certain conditions on metallic nanostructures even at excitation energies far below the energy gap between the LUMO of *p*NTP and the Fermi levels of the metals,[34,41] strongly suggesting that there must be alternative hot carrier transfer channels through which some transient reactive species are created to drive the reductive *p*NTP coupling reactions. However, the detailed mechanisms along these alternative pathways still remain unclear. Filling the knowledge gaps and clarifying the controversies mentioned above are pivotal to the establishment of generic design principles guiding rational optimization of both the nano-photocatalyst structures and the reaction conditions for plasmon-driven chemical conversions.

Here, we use surface-enhanced Raman scattering (SERS) as a plasmon-enhanced spectroscopic tool with unique molecular fingerprinting capability to resolve the detailed molecular transformations in real time during plasmon-driven reductive coupling of *p*NTP chemisorbed on Ag nanocube (NC) surfaces under near-infrared excitations in an aerobic reaction environment. Through deliberately designed SERS-based kinetic measurements, we have been able to not only gain important insights into the contribution of photothermal heating and local-field enhancement to the overall reaction kinetics but also unravel a unique role of surface-adsorbed molecular oxygen as an interfacial charge carrier-relaying cocatalyst that mediates the multistep *p*NTP coupling reaction.

■ METHODS

The dual-functional Fe_3O_4@Ag NCs core−satellites supra-nanoparticles (denoted as Fe_3O_4@Ag NC SNPs), which served as both the plasmonic photocatalysts and the SERS substrates, were assembled by attaching monodisperse Ag NCs to the surface of magnetic Fe_3O_4 microbeads through an electrostatic layer-by-layer assembly process. The details of the synthesis and structural characterizations of Fe_3O_4@Ag NC SNPs are presented in the Supporting Information. Submonolayer films of isolated Fe_3O_4@Ag NC SNPs were prepared by immobilizing the particles onto poly(4-vinylpyridine)-functionalized silicon substrates.[43−45] In a typical procedure, silicon substrates were cleaned in a piranha solution (H_2SO_4:H_2O_2, 7:3 volume ratio) for 15 min and then immersed in a 1 wt % of poly(4-vinylpyridine)−ethanol solution for 24 h. The silicon substrates were thoroughly rinsed with ethanol and dried with N_2 gas before use. Fe_3O_4@Ag NC SNPs were incubated in *p*NTP solution with various concentrations at room temperature for 1 h and then washed with ethanol and redispersed in water. The molecular coverage was controlled by incubating Fe_3O_4@Ag NC SNPs in various concentrations of *p*NTP (10 μM, 50 μM, 250 μM, and 1 mM). Then the poly(4-vinylpyridine)-functionalized silicon substrates were immersed in an aqueous solution of *p*NTP-coated Fe_3O_4@Ag NC SNPs for 1 h. The silicon substrates were thoroughly rinsed with ethanol and dried with N_2 gas after they were removed from the colloidal suspensions of *p*NTP-coated Fe_3O_4@Ag NC SNPs.

Time-resolved SERS spectra were collected by using a Bayspec Nomadic Raman microscope built on an Olympus BX51 reflected optical system under 785 nm continuous wave (CW) laser excitation in the confocal mode (focal area of 2 μm diameter). A 50× dark field objective (NA = 0.5, WD = 10.6 mm, Olympus LMPLFLN-BD) was used for both Raman signal collection and dark field scattering imaging. The laser beam was focused on one Fe_3O_4@Ag NC SNP each time for Raman spectrum collection. The laser power focused on the samples was adjusted in the range 100−1000 μW by using a neutral density filter, and the spectrum acquisition time was varied from 1 to 30 s under most experimental conditions. The time-resolved SERS measurements on *p*-aminothiophenol (*p*ATP) and thiophenol (TP) were also done in the same way. Typically, the plasmon-driven reactions occurred under ambient air at room temperature. To change the reaction media, we flowed O_2, N_2, O_2/N_2 mixtures, or water into the reaction chamber by using a flow cell with an inlet and an outlet similar to the ones we previously used for single-molecule fluorescence measurements,[46] except that the flow cell was assembled on a silicon substrate instead of a poly(ethylene glycol)-functionalized glass coverslip. The details of data analysis and density functional theory (DFT) calculations are presented in the Supporting Information.

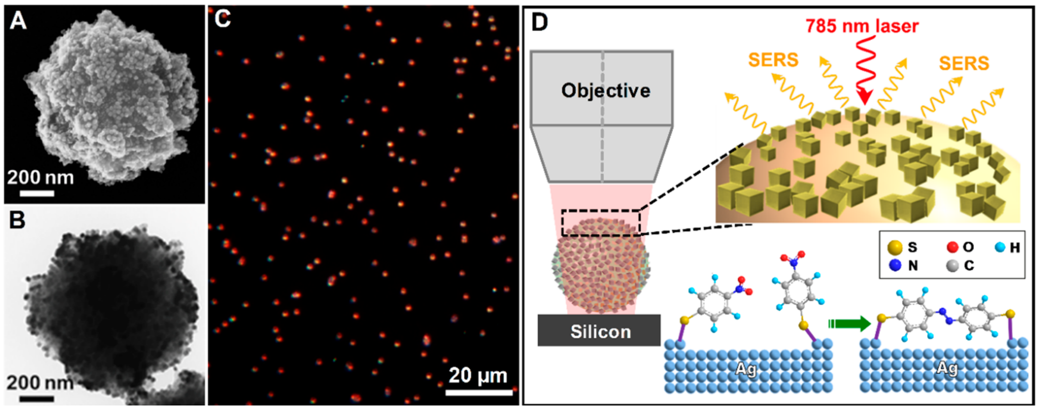

Figure 1. (A) SEM and (B) TEM images of individual Fe_3O_4@Ag NC SNPs. (C) Dark-field optical microscopy image of isolated Fe_3O_4@Ag NC SNPs on Si substrate. (D) Schematic illustration of using SERS to monitor the plasmon-driven *p*NTP coupling on Fe_3O_4@Ag NC SNPs.

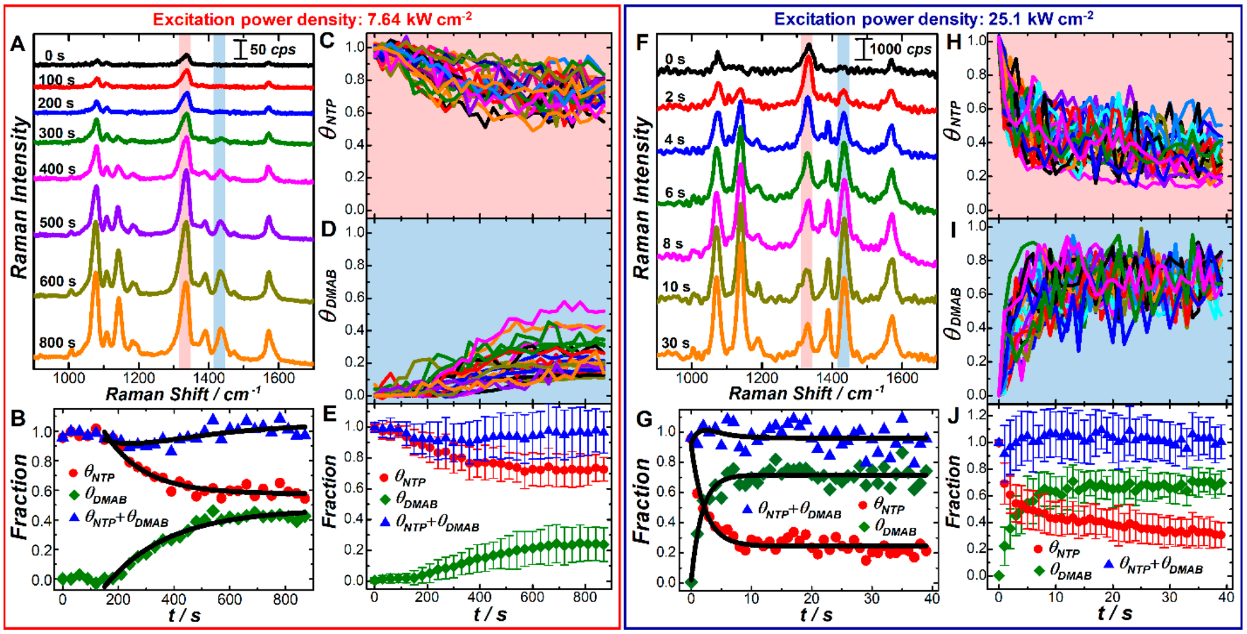

Figure 2. Temporal evolutions of (A) SERS spectra and (B) θ_{NTP}, θ_{DMAB}, and $\theta_{DMAB} + \theta_{NTP}$ on one *p*NTP-coated Fe_3O_4@Ag NC SNP (λ_{ex}: 785 nm; ρ_{ex}: 7.64 kW cm^{-2}). The SERS spectra are offset for clarity, and the Raman intensities are shown by using counts per second (cps) as the unit. Trajectories of (C) θ_{NTP} and (D) θ_{DMAB} collected on 22 individual *p*NTP-coated Fe_3O_4@Ag NC SNPs. (E) Ensemble-averaged θ_{NTP}, θ_{DMAB}, and $\theta_{DMAB} + \theta_{NTP}$ trajectories. Temporal evolutions of (F) SERS spectra and (G) θ_{NTP}, θ_{DMAB}, and $\theta_{DMAB} + \theta_{NTP}$ on one *p*NTP-coated Fe_3O_4@Ag NC SNP (λ_{ex}: 785 nm; ρ_{ex}: 25.1 kW cm^{-2}). Trajectories of (H) θ_{NTP} and (I) θ_{DMAB} collected on 25 individual *p*NTP-coated Fe_3O_4@Ag NC SNPs. (J) Ensemble-averaged θ_{NTP}, θ_{DMAB}, and $\theta_{DMAB} + \theta_{NTP}$ trajectories. The θ_{NTP} and θ_{DMAB} trajectories are fitted by using the first-order rate equations, and the curve fitting results are shown as solid curves in panels B and G.

■ RESULTS AND DISCUSSION

We constructed dual-functional Fe_3O_4@Ag NC SNPs, which served as both the plasmonic photocatalysts and the SERS substrates, by decorating the surface of magnetic Fe_3O_4 microbeads (1 μm in diameter, Figure S1 in the Supporting Information) with monodisperse Ag NCs[47] (average edge length of 36 nm, Figure S2). Because the surfaces of carboxylate-functionalized Fe_3O_4 beads and poly(vinylpyrrolidone)-capped Ag NCs were both negatively charged, we used a thin layer of positively charged poly(diallyldimethylammonium chloride) (PDDA) as the spacer between the Fe_3O_4 beads and Ag NCs to assemble the Fe_3O_4@Ag NC SNPs electrostatically through a layer-by-layer assembly process[48,49] (Figure S3A,B). The coverage density of Ag NCs on the Fe_3O_4 surfaces progressively increased upon repeated incubation of PDDA-coated Fe_3O_4 beads with colloidal Ag NCs for multiple times (Figure S3C−F), and each time, the Fe_3O_4@Ag NC SNPs could be trapped and separated from the colloidal Ag NCs simply by using a magnet benefiting from the intrinsic magnetic properties of the Fe_3O_4 beads. Figures 1A and 1B show the scanning electron microscopy (SEM) and transmission electron microscopy (TEM) images, respectively, of individual Fe_3O_4@Ag NC SNPs synthesized after incubating PDDA-coated Fe_3O_4 beads with colloidal Ag NCs for four times. A lower magnification SEM image revealing the overall morphology and uniformity of the SNPs is shown in Figure S4. The surface of each Fe_3O_4 bead was decorated with patchy islands composed of densely packed monolayer Ag NCs. The strong plasmon coupling among neighboring Ag NCs resulted in a broad-band plasmon resonance spanning much of the visible and near-infrared regions,[21,48,50] enabling us to use a near-infrared laser for

DOI: 10.1021/acs.jpcc.9b08181
J. Phys. Chem. C 2019, 123, 26695−26704

plasmonic excitation to create "hot spots" in the gaps between adjacent NCs, which were exploited not only for Raman signal enhancement but also for hot electron generation. After forming self-assembled monolayers of *p*NTP on Ag surfaces, the *p*NTP-coated Fe_3O_4@Ag NC SNPs were dispersed on a Si substrate as isolated particles with typical interparticle distances beyond a few micrometers (Figure 1C). As illustrated in Figure 1D, a CW excitation laser was focused onto a focal spot that was ~2 μm in diameter by using a confocal Raman microscope, which allowed us to correlate detailed molecular transformations and reaction kinetics with local-field intensities at the single SNP level.

We focused the laser on one *p*NTP-coated Fe_3O_4@Ag NC SNP each time to continuously monitor the plasmon-driven molecular transformations until completion of the reactions using SERS as an *in situ* spectroscopic tool. Figure 2A shows the temporal evolution of SERS spectral features under ambient air at an excitation wavelength (λ_{ex}) of 785 nm and excitation power density (ρ_{ex}) of 7.64 kW cm^{-2}. The entire reaction process could be divided into two stages. At the initial stage, three SERS peaks at 1572, 1338, and 1078 cm^{-1} were clearly resolved, corresponding to the characteristic aromatic ring stretching (ν_{ring}), symmetric nitro stretching (ν_{NO_2}), and C−S bond stretching (ν_{C-S}) modes of *p*NTP, respectively.[30,38,51] We observed an induction time lasting ~150 s during which all the Raman peaks of *p*NTP were well-preserved without any spectral signatures of DMAB observable in the SERS spectra. Following this induction time, three new Raman peaks signifying the formation of DMAB emerged at 1438, 1142, and 1390 cm^{-1},[19,38,48] all of which became progressively more intense as the coupling reaction proceeded. Multiple SERS peaks became significantly stronger upon DMAB formation because the Raman cross sections of DMAB were much larger than those of *p*NTP.[52]

We calculated the apparent fractions of DMAB and *p*NTP, denoted as θ_{DMAB} and θ_{NTP}, respectively, at particular reaction times, *t*, based on the relative intensities of the SERS peaks at 1438 cm^{-1} ($\nu_{N=N}$ of DMAB) and 1338 cm^{-1} (ν_{NO_2} of *p*NTP) with respect to the ν_{ring} mode at 1572 cm^{-1} (see details in the Supporting Information). An alternative way to produce DMAB involves plasmon-driven oxidative coupling of *p*-aminothiophenol (*p*ATP) under aerobic conditions.[19,48,53] After being continuously illuminated by 785 nm laser at a ρ_{ex} of 11.8 kW cm^{-2} for 150 s, *p*ATP molecules adsorbed on Fe_3O_4@Ag NC SNPs were converted into DMAB with nearly 100% yield (Figure S5), which was set as the reference state for θ_{DMAB} of 100%. As shown in Figure 2B, the temporal evolutions of θ_{DMAB} and θ_{NTP} both obeyed an apparent first-order rate law, which could be described by the following rate equations:

$$\theta_{DMAB}(t) = \theta_{t=\infty}[1 - e^{-k(t-t_{ind})}] \tag{1}$$

and

$$\theta_{NTP}(t) = 1 - \theta_{t=\infty} + \theta_{t=\infty}e^{-k(t-t_{ind})} \tag{2}$$

where *k* is the apparent first-order rate constant, $\theta_{t=\infty}$ is the maximum yield of DMAB achievable at infinitely long reaction time, and t_{ind} refers to the duration of induction time. The three key parameters could be obtained by performing least-squares curve fitting to the experimental results. No spectral features corresponding to any reaction intermediates were resolvable under the current experimental conditions, and the sum of θ_{NTP} and θ_{DMAB} remained very close to unity during the entire reaction process (Figure 2B). Similar spectral evolution and reaction kinetics were observed when the SERS-based kinetic measurements were repeated on 22 different Fe_3O_4@Ag NC SNPs one particle at a time under identical reaction conditions (Figures 2C−E). When increasing ρ_{ex} to 25.1 kW cm^{-2}, the reductive coupling of *p*NTP on Fe_3O_4@Ag NC SNPs became kinetically much faster but still proceeded following the first-order rate law (Figures 2F−J). A significantly higher $\theta_{t=\infty}$ was achieved, while t_{ind} became so short that it was experimentally irresolvable. The *p*NTP coupling kinetics was intimately tied to the plasmonic properties of the Ag NC satellites with no observable contribution from the magnetic properties of Fe_3O_4 cores, as confirmed by the control experiments in which we substituted the Fe_3O_4 cores with dielectric SiO_2 beads (1 μm in diameter) while keeping the surface coverage of Ag NCs nominally the same (Figure S6).

Multiple experimental observations coherently suggested that *p*NTP adsorbed on Ag surfaces underwent photothermally driven changes in their adsorption conformations without forming DMAB during the induction time. First, increasing ρ_{ex} led to shortening of t_{ind} because of faster and more efficient photothermal heating at the particle surfaces. Second, thermal treatment of the *p*NTP-coated Fe_3O_4@Ag NC SNPs at 120 °C for 30 min prior to laser illumination also resulted in shortening of t_{ind} (Figure S7). Third, the conformational changes of *p*NTP adsorbates were well-reflected by SERS spectral evolution during the induction time, which witnessed progressive intensification and slight frequency upshift of the characteristic *p*NTP SERS peaks (Figure 2A). Such increase of peak intensities and upshift of the peak positions were also observed in the SERS spectra when the *p*NTP-coated Fe_3O_4@Ag NC SNPs were thermally treated at 120 °C without laser illumination (Figure S8). Fourth, after heating the sample at 120 °C for 30 min, no characteristic DMAB SERS peaks emerged, further verifying that the reductive coupling of *p*NTP was essentially a plasmon-driven photoreaction rather than a thermally driven process. Recent studies revealed that the plasmon-driven reductive coupling of *p*NTP on Au and Ag substrates required the alignment of *p*NTP molecules toward specific orientations with respect to the metal surfaces.[54] The thermal relaxation of *p*NTP adsorbates to their lowest energy adsorption conformation, which resulted in an enthalpy decrease compensating for the entropy loss caused by the molecular alignment, appeared to be a thermodynamic prerequisite for the *p*NTP coupling reaction. Our experimental results were further corroborated by density functional theory (DFT) calculations. Three adsorption conformations were identified by DFT calculations when a *p*NTP molecule was covalently linked to an atomic cluster composed of three Ag atoms through Ag−S interactions to form a compound denoted as Ag_3-*p*NTP (Figure S9A). The energies of various adsorption conformations differed by a few hundred cal mol^{-1}, which were commensurate with the room-temperature thermal fluctuation (0.59 kcal mol^{-1}). When the adsorption of *p*NTP to Ag surfaces occurs at room temperature, *p*NTP may adopt several different adsorption conformations, some of which represent kinetically trapped metastable states. Under laser illumination at the power densities typically used for SERS measurements, the local temperature at the particle surfaces was estimated to increase by several tens of degrees[34] or even more,[37] which provided sufficient thermal energy to overcome

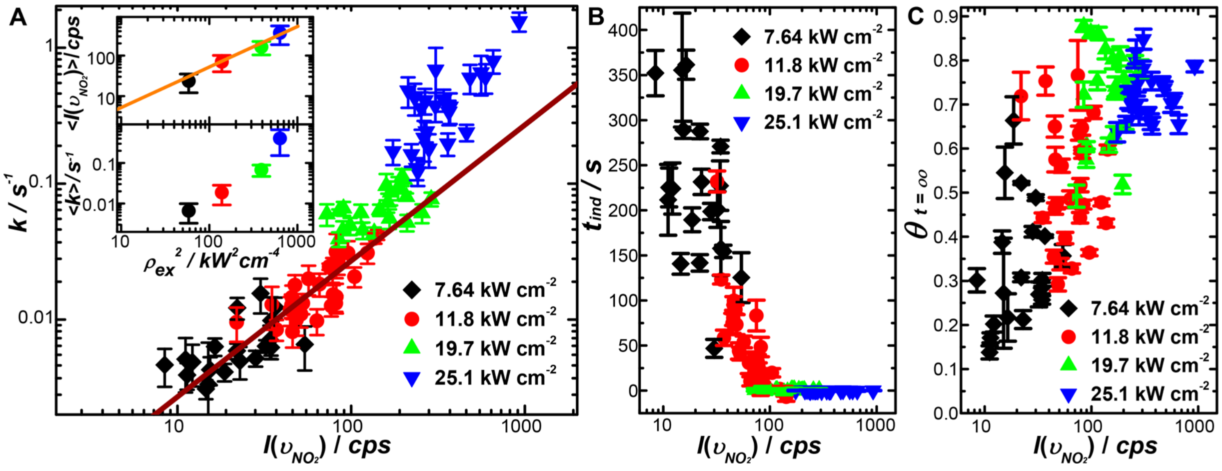

Figure 3. Plots of (A) k, (B) t_{ind}, and (C) $\theta_{t=\infty}$ versus the initial peak intensities of the ν_{NO_2} mode, $I(\nu_{NO_2})$. The λ_{ex} was fixed at 785 nm, while the ρ_{ex} was varied. At each ρ_{ex}, the time-resolved SERS measurements were repeated on more than 20 individual Fe_3O_4@Ag NC SNPs one particle at a time. The k values obtained at 7.64 and 11.8 kW cm^{-2} exhibited a linear relationship to $I(\nu_{NO_2})$, and the fitting results are shown as a solid line in panel A. The inset of panel A shows ensemble averaged $I(\nu_{NO_2})$ (upper panel) and k (lower panel) as a function of ρ_{ex}^2.

the activation energy barriers for the conformational changes. The experimentally observed upshift of the Raman peaks was also reproduced by DFT calculations when a *p*NTP adsorbate switched from a metastable state to its lowest energy adsorption conformation (Figure S9B). The DFT results, however, did not accurately predict the relative intensities of various SERS peaks because DFT essentially calculated the normal Raman spectra of the Ag_3-*p*NTP compound rather than SERS of *p*NTP adsorbed on a plasmonic substrate.

To more conclusively draw the connections between photothermal heating and conformational changes of thiolated aromatic adsorbates on Ag, we tracked the SERS spectral evolution of thiophenol (TP) adsorbed on Fe_3O_4@Ag NC SNPs under continuous laser illumination. Using TP as the probe molecule instead of *p*NTP allowed us to study the photothermally induced conformational changes without the complication by plasmon-driven coupling reactions. Analogous to *p*NTP, TP also chemisorbs on Ag surfaces through covalent Ag−S interactions, as evident by the absence of the Raman signatures of S−H bond stretching at 2560 and 920 cm^{-1} in the SERS spectra (Figure S10). Comparing the normal Raman and the SERS spectral features, we found that the chemisorption of TP on Ag surfaces resulted in frequency downshifts of both the ν_{C-S} and ν_{ring} modes. After illuminating a TP-coated Fe_3O_4@Ag NC SNP by a laser (785 nm, 25.1 kW cm^{-2}), the SERS peaks corresponding to the ν_{C-S} and ν_{ring} modes both further downshifted by ∼5 cm^{-1}, indicating the strengthening of the metal−molecule interactions[55] (Figures S10). We repeated the same measurements on multiple TP-coated Fe_3O_4@Ag NC SNPs and observed essentially the same phenomenon. The laser illumination also caused the SERS peak intensity of the ν_{C-S} mode to increase by ∼2.5 times (Figure S11). Both the ν_{C-S} and ν_{ring} modes also experienced a frequency downshift by ∼5 cm^{-1}, and the SERS peak intensity of the ν_{C-S} mode increased significantly after thermally heating the TP-coated Fe_3O_4@Ag NC SNPs at 120 °C for 30 min (Figure S12), in line with previous observations.[55] DFT results showed that there were three conformations of the Ag_3-TP compound (Figure S13). Upon transition from a metastable conformation to the lowest energy conformation, both the ν_{C-S} and ν_{ring} modes exhibited frequency downshifts, in agreement with our experimental observations.

The SERS-based kinetic measurements provided a unique way for us to correlate the reaction kinetics with the local field intensities. The magnitude of local field (|E|) can be tuned either by adjusting ρ_{ex}, which is proportional to the square of the electric field intensity of the excitation light (|E_0|^2), or by varying the local-field enhancement (|E|/|E_0|), which is λ_{ex}-dependent and intimately tied to the structural and plasmonic features of the nano-photocatalysts. We collected SERS data at four different ρ_{ex} of 7.64, 11.8, 19.7, and 25.1 kW cm^{-2}, respectively. At each ρ_{ex}, we repeated the SERS measurements on more than 20 different *p*NTP-coated Fe_3O_4@Ag NC SNPs one particle at a time. The initial SERS intensities of the characteristic ν_{NO_2} mode of *p*NTP, $I(\nu_{NO_2})$, varied from particle to particle due to the intrinsic variations in the distribution, densities, and field enhancements of the hot spots among different SNPs. It is well-known that the Raman enhancement of a molecular adsorbate is proportional approximately to the fourth power of the local-field enhancement, (|E|/|E_0|)^4, at the surface sites where the molecule resides.[56] For a molecule located in the close vicinity of an individual plasmonic nanoparticle with a moderate local-field enhancement, its SERS intensity is typically proportional to the power density of the incident laser (ρ_{ex}), or |E_0|^2. However, if molecules are located inside the gap between multiple strongly coupling plasmonic nanostructures, their SERS intensity has been observed to exhibit a quadratic dependence on the incident laser power when ρ_{ex} is on the order of 10 kW cm^{-2}.[57] Such an ρ_{ex}^2 dependence of the SERS intensity can be interpreted in the context of enhanced nonlinear polarization mechanisms.[57] On the Fe_3O_4@Ag NC SNPs, the majority of the SERS signals came from those molecules located inside the gaps between the adjacent, strongly coupled Ag NCs. As shown in the inset of Figure 3A, the ensemble-averaged $I(\nu_{NO_2})$ at each ρ_{ex} increased linearly with ρ_{ex}^2. In contrast, the ensemble-averaged values of rate constant, ⟨k⟩, apparently exhibited a superlinear relationship to ρ_{ex}^2.

In Figure 3A, we plotted k as a function of $I(\nu_{NO_2})$ at various ρ_{ex} obtained on individual *p*NTP-coated Fe_3O_4@Ag NC SNPs.

DOI: 10.1021/acs.jpcc.9b08181
J. Phys. Chem. C 2019, 123, 26695−26704

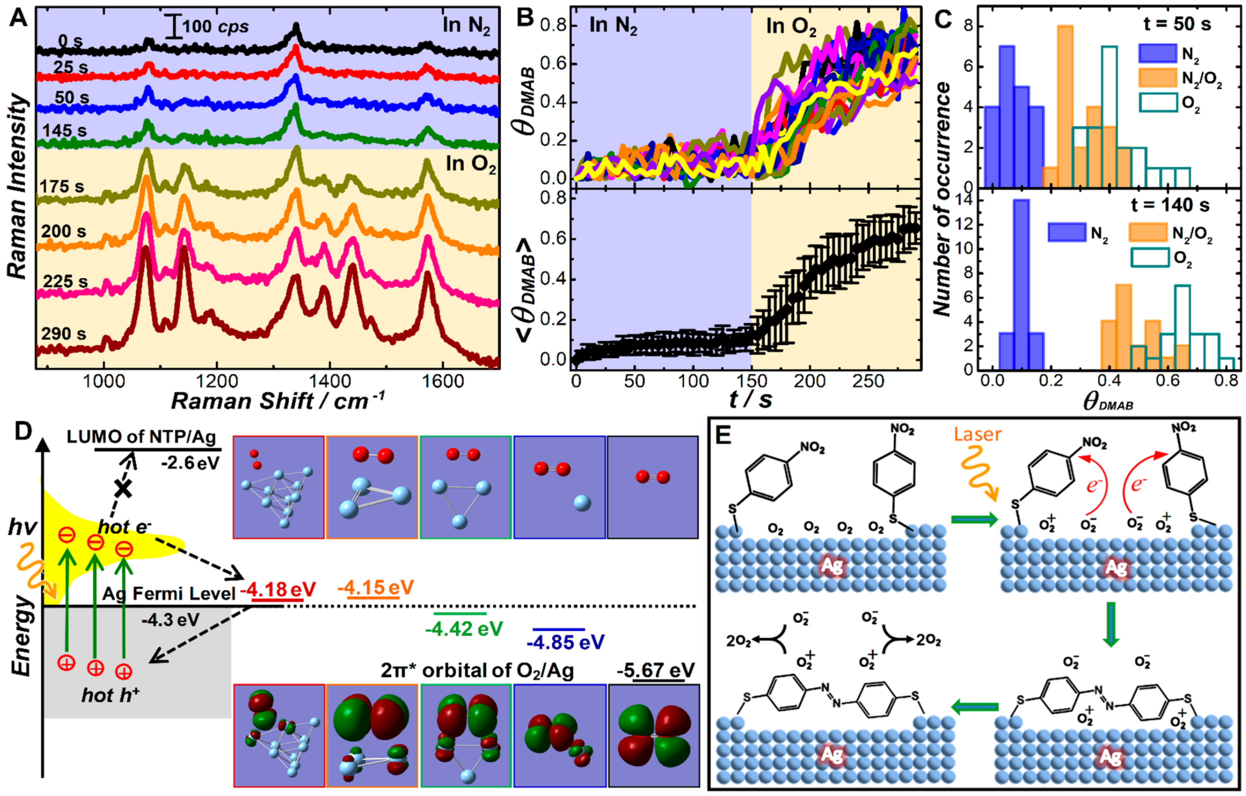

Figure 4. (A) Temporal evolution of SERS spectra on one *p*NTP-coated Fe_3O_4@Ag NC SNP, (B) θ_{DMAB} trajectories of 20 individual *p*NTP-coated Fe_3O_4@Ag NC SNPs and ensemble-averaged θ_{DMAB} trajectory in varying reaction atmospheres. The λ_{ex} is 785 nm, and the ρ_{ex} is 16.9 kW cm^{-2}. During the first 150 s upon laser illumination, the molecules were exposed to N_2. Then the reaction atmosphere was switched to O_2. (C) Distribution of θ_{DMAB} at reaction times of (upper panel) 50 s and (lower panel) 140 s for *p*NTP-coated Fe_3O_4@Ag NC SNPs in N_2, O_2, and mixed N_2/O_2 (1:1 volume ratio) atmospheres. The total pressure is 1 atm. (D) Energy diagram illustrating the plasmonic hot carrier transfers involved in the reductive coupling of *p*NTP aided by interfacial O_2 under near-infrared excitations. The energy levels of the 2π* of O_2 adsorbed on Ag atomic clusters were calculated by DFT. The energy diagram is plotted by using an energy scale of electronvolts (eV) and the vacuum level as the reference. The optimized geometries and the electron density maps of 2π* orbital of an O_2 molecule adsorbed on an Ag atom, an Ag_3 cluster, and an Ag_{10} cluster are shown above and below the orbital energy levels, respectively. (E) Proposed mechanism of plasmon-driven aerobic reductive coupling of *p*NTP chemisorbed on Ag.

In the low ρ_{ex} regime (7.64 and 11.8 kW cm^{-2}), k was observed to be proportional to $I(\nu_{NO_2})$, clearly showing that the reaction rate scaled with $(|E|/|E_0|)^4$. When we plotted k as a function of square root of $I(\nu_{NO_2})$, or in other words, $(|E|/|E_0|)^2$, such a linear relationship was not observed (Figure S14). Interestingly, when ρ_{ex} increased to 19.7 kW cm^{-2}, k started to deviate significantly from the linear relationship with respect to $I(\nu_{NO_2})$, and a superlinear dependence was observed. At low ρ_{ex}, the photothermal effect was rather insignificant, and the photogenerated hot carriers provided the major contribution to the overall reaction kinetics. In the high ρ_{ex} regime, however, the photothermal heating became a significant effect, further kinetically boosting the *p*NTP coupling reaction and causing k to exhibit a superlinear dependence. The photothermal effect became progressively more pronounced as $|E|$ increased. As a consequence, t_{ind} was observed to decrease as $|E|$ increased in the low ρ_{ex} regime (Figure 3B). At ρ_{ex} of 19.7 and 25.1 kW cm^{-2}, the photothermal effect became so pronounced that the t_{ind} values approached 0. It is worth mentioning that it is difficult, if not at all impossible, to completely separate the contributions of local-field enhancements and photothermal heating because the photothermal effect is intimately tied to the enhancement of local electromagnetic fields as well. The deviation from the linear relationship in the plots of k vs $I(\nu_{NO_2})$ observed in the high ρ_{ex} regime strongly suggested that the photothermal heating effect played a key role in boosting the reactions at high excitation powers.

Interestingly, the photothermal heating also exhibited remarkable influence on $\theta_{t=\infty}$. As shown in Figure 3C, $\theta_{t=\infty}$ gradually increased with $|E|$ until reaching a plateau value around 80%. The plasmon-driven *p*NTP coupling was observed to be an irreversible reaction under our experimental conditions. The reverse reaction, decoupling of DMAB, was so slow that it became experimentally unobservable even in the absence of laser illumination. Once the DMAB molecules were produced, their characteristic SERS features were well-preserved without any observable photodegradation under continuous laser illumination (Figure 2). Therefore, the partial conversion of *p*NTP to DMAB could be most reasonably explained by the presence of a subpopulation of unreactive *p*NTP adsorbed on the Ag surfaces. However, this unreactive subpopulation may be thermally activated by plasmonic photothermal heating, causing $\theta_{t=\infty}$ to increase with $|E|$ on the photocatalyst surfaces. As shown in Figure S7, thermal annealing of *p*NTP-coated Fe_3O_4@Ag NC SNPs at 120 °C prior to laser illumination resulted in not only the shortening of t_{ind} but also increase of $\theta_{t=\infty}$.

An alternative way to tune $|E|$ is to vary the coverage of Ag NCs on the Fe_3O_4 beads. Increasing the coverage of Ag NCs not only increased the density of hot spots on each SNPs but also resulted in higher field enhancements ($|E|/|E_0|$) in the hot spots due to decreased average distances between neighboring NCs. On the Fe_3O_4@Ag NC SNPs synthesized after four cycles of incubation (Fe_3O_4@Ag-4), we observed significantly higher k and $\theta_{t=\infty}$ but shorter t_{ind} than those on the Fe_3O_4@Ag NC SNPs synthesized after incubation for only once (Fe_3O_4@Ag-1). Surprisingly, when a saturated Au NC coverage was achieved after seven cycles of incubation (Fe_3O_4@Ag-7), both k and $\theta_{t=\infty}$ decreased even though $|E|$ and $I(\nu_{NO_2})$ became even stronger (Figure S15). It was highly likely that at this saturated Ag NC coverage the gaps between neighboring NCs became so small that the surface-adsorbed *p*NTP molecules experienced a locally crowded environment, which imposed steric hindrance on *p*NTP to suppress the coupling reaction. It was also possible that this coupling reaction involved the participation of other molecular species in the atmosphere, which had restricted access to the hot spots confined within the tiny gaps among close-packed Ag NCs. We further systematically tuned the molecular coverage of *p*NTP on Ag by incubating Fe_3O_4@Ag-4 particles with *p*NTP at four different concentrations (10 μM, 50 μM, 250 μM, and 1 mM) to investigate the effect of molecular coverage on the reaction kinetics. Based on our estimates (see details in the Supporting Information), a saturated monolayer coverage of *p*NTP on Ag surfaces was achieved at *p*NTP concentrations of 250 μM and 1 mM, whereas submonolayers of *p*NTP formed on Ag surfaces at *p*NTP concentrations of 10 and 50 μM. As shown in Figure S16, both k and $\theta_{t=\infty}$ increased with the molecular coverage of *p*NTP on Ag because the formation of DMAB required *p*NTP molecules in close proximity to each other. However, t_{ind} appeared independent of *p*NTP coverage on Ag, suggesting that the photothermal heating of the particle surfaces triggered the conformational changes rather than causing surface migration of the molecular adsorbates during the induction time.

While both photothermal heating and local-field enhancements profoundly influenced the overall reaction kinetics, the most essential driving force for the reductive *p*NTP coupling was the plasmonic hot carriers. It has been shown that when the excitation energy exceeds the energy gap between the LUMO of surface-adsorbed *p*NTP and the Ag Fermi level, the plasmonic hot electrons in Ag nanoparticles can be injected into *p*NTP to initiate the reductive coupling of *p*NTP into DMAB.[35,38] The injection of a hot electron into *p*NTP results in spectral downshift of the ν_{NO_2} SERS peak by up to 5 cm^{-1}, which signifies the formation of a transient anionic *p*NTP radical.[38] Under our experimental conditions, the hot electrons were distributed in the energy range from the Ag Fermi level (−4.3 eV vs vacuum) up to ~1.58 eV above the Ag Fermi level because we used a 785 nm laser for plasmon excitations. Therefore, the hot electrons were expected to have insufficient energy to transfer into the LUMO of *p*NTP chemisorbed on Ag surfaces (~1.7 eV above the Ag Fermi level). In our experiments, no spectral downshift of the ν_{NO_2} mode was observed, indicating that the reductive *p*NTP coupling reaction occurred along alternative hot carrier transfer pathways and some species in the reaction atmosphere may serve as the hot carrier-relaying units to dynamically maneuver the reaction kinetics.

We performed the SERS-based kinetics measurements in a series of controlled reaction atmospheres to identify the possible hot carrier-relaying species in the ambient air. When the *p*NTP-coated Fe_3O_4@Ag NC SNPs were exposed to pure N_2, no coupling reaction was observed at ρ_{ex} of 16.9 kW cm^{-2} even after 150 s (t_{ind} was very close to 0 s at this ρ_{ex} under ambient air), and the characteristic *p*NTP SERS peaks became progressively more intense and slightly upshifted as a consequence of photothermally induced *p*NTP conformational changes under continuous laser illumination. The *p*NTP started to undergo fast coupling reactions to form DMAB immediately after we switched the reaction atmosphere from N_2 to pure O_2 (Figures 4A,B). We further studied the reaction kinetics in a reaction atmosphere composed of both N_2 and O_2 mixed at 1:1 volume ratio (Figure S17). In Figure 4C, we compared the θ_{DMAB} at reaction times of 50 and 140 s in N_2, O_2, and N_2/O_2 mixed atmospheres. Apparently, O_2 played a crucial role in boosting this reaction, while N_2 was essentially inert. Water was also found to be an inert medium for this plasmon-driven reaction with only limited amount of DMAB produced under laser illumination when the *p*NTP-coated Fe_3O_4@Ag NC SNPs were exposed to water (Figure S18) primarily due to the molecular O_2 dissolved in water.

Molecular O_2 adsorbed on plasmonic nanoparticle surfaces has been identified as an important hot electron acceptor in several plasmon-driven oxidation reactions.[15,16,48,53] The hot electron transfer from metals to surface-adsorbed O_2 results in the formation of transient, highly reactive O_2^- radicals that are capable of selectively oxidizing a variety of molecular adsorbates.[15,16,44,49] At first glance, the crucial role of O_2 we observed in this reductive coupling reaction seems surprising and puzzling. However, deliberation on the energy alignment between the frontier orbitals of surface-adsorbed O_2 and the Fermi level of Ag allowed us to get a clear picture on the hot carrier channeling mechanisms. The partially filled $2\pi^*$ orbitals represent the frontier molecular orbitals of O_2, which are doubly degenerate and antibonding in nature. DFT calculations showed that the energy of the $2\pi^*$ orbital of free O_2 was significantly lower than the Fermi level of Ag (Figure 4D). The absorption of an O_2 molecule to an Ag atomic cluster positively shifted the energy of the $2\pi^*$ orbital toward the Ag Fermi level. On an Ag_{10} cluster, the energy of the $2\pi^*$ orbital of O_2 became very close to the Ag Fermi level, which was in agreement with the energy of O_2 adsorbed on an Ag {100} facet (the crystallographic facets exposed on Ag NC surfaces) predicted by DFT calculations.[15] The energetically favorable alignment of $2\pi^*$ orbital of O_2 with respect to Ag Fermi level facilitated the transfer of a hot electron from Ag to the $2\pi^*$ orbital of O_2 to generate an O_2^- radical, which might rapidly pass an electron onto surface-adsorbed *p*NTP to initiate the reductive coupling reaction and regenerate O_2. Considering the charge balance, two O_2^- radicals are released after two anionic *p*NTP radicals are coupled to produce one DMAB molecule. Meanwhile, the electrons in the $2\pi^*$ orbital of surface-adsorbed O_2 might also migrate into the Ag to combine with the plasmonic holes, preventing the Ag NCs from photocorrosion during the reactions. Both the interfacial O_2^- and O_2^+ radicals were short-lived, undergoing rapid recombination to form O_2. Figure 4E schematically illustrates the key steps involved in our proposed reaction mechanism. In this plasmon-driven molecule-transforming process, O_2 essentially played a unique role as a hot carrier-relaying cocatalyst that worked synergistically with the plasmonic Ag photocatalysts. The plasmon-driven reductive coupling of *p*NTP is a mechanistic complex, multistep reaction involving multiple

DOI: 10.1021/acs.jpcc.9b08181
J. Phys. Chem. C 2019, 123, 26695−26704

transient intermediates along the reaction pathways. Although none of these short-lived intermediates were spectroscopically resolvable by SERS under our experimental conditions, we found that the overall reaction kinetics was determined by one rate-limiting step and thus could be well-described by an apparent first-order rate law.

Our observations were in striking contrast to previous work done by Xu and co-workers,[32] who found that the plasmon-driven reductive coupling of *p*NTP occurred rapidly on Ag nanoparticles in a N_2 atmosphere but became kinetically much slower in an O_2 atmosphere at $\lambda_{ex} = 633$ nm. Visible excitations created a population of the hot electrons that had sufficient energy to get injected into the LUMO of surface-adsorbed *p*NTP to initiate the coupling reaction. The presence of O_2 in the reaction atmosphere suppressed the hot electron injection into *p*NTP and consequently impeded the conversion of *p*NTP to DMAB because O_2 competed with *p*NTP for hot electrons. However, in our case, the coupling of *p*NTP occurred along a distinct pathway involving the photoactivation of interfacial O_2 through hot electron transfer from the Ag nanoparticles to surface-adsorbed O_2, which essentially interpreted why an aerobic environment was so crucial to this plasmon-driven coupling reaction under near-infrared excitations. While our experimental observations and DFT calculations coherently suggest the crucial roles of O_2^- and O_2^+ radicals in the plasmon-driven *p*NTP coupling reaction under near-infrared excitations, it still remains challenging to spectroscopically resolve these transient reactive species because of their short lifetimes, low abundance at the nanoparticle surfaces, and intrinsically small Raman cross sections. Although experimentally challenging, obtaining direct evidence on the formation of transient O_2^- and O_2^+ radicals on the nanoparticle surfaces will be a critical step toward the further validation of the proposed mechanisms.

■ CONCLUSIONS

In summary, the photocatalytic reductive coupling of *p*NTP on nanostructured Ag surfaces under aerobic reaction conditions serves as a model reaction ideal for elucidating the photothermal effect, local-field dependence, and hot carrier-channeling mechanisms of plasmon-driven photocatalysis. Our time-resolved SERS results help clarify several mechanistic ambiguities widely debated in the plasmonic photocatalysis communities and provide compelling experimental evidence clearly showing that both plasmonic photothermal effect and local field enhancement play crucial roles in kinetically boosting plasmon-driven chemical transformations on metallic nanostructure surfaces. As exemplified by this work, the reaction rate scales proportionally to $|E|^4$ in the low ρ_{ex} regime when the reaction kinetics is predominantly determined by plasmonic hot carriers with a rather insignificant contribution from the photothermal effect. However, the photothermal effect becomes increasingly more pronounced as ρ_{ex} increases, giving rise to a superlinear dependence of the rate constant on $|E|^4$. The photothermal heating at the nanoparticle surfaces also triggers the transitions of *p*NTP adsorbates from metastable states to thermodynamically most stable conformations, thereby activating the surface-adsorbed *p*NTP for the reductive coupling reactions. Such conformational changes of molecular adsorbates triggered by plasmonic photothermal heating at the molecule−nanoparticle interfaces is experimentally witnessed as an induction time at the early stage before the coupling reaction occurs. Although hot electron transfer from Ag to *p*NTP adsorbates is energetically unfavorable under near-infrared excitations, the hot electron transfer occurs through an alternative channel involving the surface-adsorbed molecular O_2 as a unique hot carrier relaying cocatalyst that works synergistically with the plasmonic Ag catalysts to mediate the multistep reductive coupling reaction. The insights gained from this work provide a solid knowledge foundation for us to extract key design principles that guide us to rationally tune the plasmonic properties of nano-photocatalysts and judiciously tailor the local reaction environment at the nanoparticle−molecule interfaces toward optimization of plasmon-driven chemical transformations.

■ ASSOCIATED CONTENT

Supporting Information

The Supporting Information is available free of charge on the ACS Publications website at DOI: 10.1021/acs.jpcc.9b08181.

> Additional experimental details, details of DFT calculations, estimates of molecular coverage of *p*NTP on Ag surfaces, and additional figures including TEM images, SEM images, ζ-potential results, DFT results, SERS spectra, and kinetic results (PDF)

■ AUTHOR INFORMATION

Corresponding Author

*E-mail wang344@mailbox.sc.edu; Ph 803-777-2203; Fax 803-777-9521.

ORCID

Qingfeng Zhang: 0000-0002-7004-9040
Yadong Zhou: 0000-0003-3357-3553
Xiaoqi Fu: 0000-0003-1029-4017
Shengli Zou: 0000-0003-1302-133X
Hui Wang: 0000-0002-1874-5137

Notes

The authors declare no competing financial interest.

■ ACKNOWLEDGMENTS

This work was supported by the University of South Carolina (USC) Office of Vice President for Research through an ASPIRE-I Track-I Award and the National Science Foundation through Awards OIA-1655740 and DMR-1253231. Q.Z. was partially supported by a USC NanoCenter Dissertation Fellowship. E.V. was partially supported by a Graduate Assistance in Areas of National Need (GAANN) Fellowship through Award P200A120075. As a visiting postdoctoral scholar, X.F. was partially supported by the Study-Abroad Funds of Jiangsu University (20162673). S.Z. acknowledges the Extreme Science and Engineering Discovery Environment (XSEDE) Open Science Grid (OSG) as the service provider through allocation szou. H.W. acknowledges Jiangsu University for Jinshan Distinguished Professorship (Short-Term Visiting Program). This work made use of the facilities at the USC Electron Microscopy Center and W.M. Keck Open Laboratory.

■ REFERENCES

(1) Brongersma, M. L.; Halas, N. J.; Nordlander, P. Plasmon-Induced Hot Carrier Science and Technology. *Nat. Nanotechnol.* **2015**, *10*, 25−34.

(2) Kale, M. J.; Avanesian, T.; Christopher, P. Direct Photocatalysis by Plasmonic Nanostructures. *ACS Catal.* **2014**, *4*, 116−128.

(3) Linic, S.; Christopher, P.; Ingram, D. B. Plasmonic-Metal Nanostructures for Efficient Conversion of Solar to Chemical Energy. *Nat. Mater.* **2011**, *10*, 911−921.

(4) Christopher, P.; Moskovits, M. Hot Charge Carrier Transmission from Plasmonic Nanostructures. *Annu. Rev. Phys. Chem.* **2017**, *68*, 379−398.

(5) Linic, S.; Aslam, U.; Boerigter, C.; Morabito, M. Photochemical Transformations on Plasmonic Metal Nanoparticles. *Nat. Mater.* **2015**, *14*, 567−576.

(6) Zhang, Y. C.; He, S.; Guo, W. X.; Hu, Y.; Huang, J. W.; Mulcahy, J. R.; Wei, W. D. Surface-Plasmon-Driven Hot Electron Photochemistry. *Chem. Rev.* **2018**, *118*, 2927−2954.

(7) Willets, K. A.; Van Duyne, R. P. Localized Surface Plasmon Resonance Spectroscopy and Sensing. *Annu. Rev. Phys. Chem.* **2007**, *58*, 267−297.

(8) Kneipp, K.; Kneipp, H.; Kneipp, J. Surface-Enhanced Raman Scattering in Local Optical Fields of Silver and Gold Nanoaggregatess - from Single-Molecule Raman Spectroscopy to Ultrasensitive Probing in Live Cells. *Acc. Chem. Res.* **2006**, *39*, 443−450.

(9) Lal, S.; Grady, N. K.; Kundu, J.; Levin, C. S.; Lassiter, J. B.; Halas, N. J. Tailoring Plasmonic Substrates for Surface Enhanced Spectroscopies. *Chem. Soc. Rev.* **2008**, *37*, 898−911.

(10) Moskovits, M. Surface-Enhanced Raman Spectroscopy: A Brief Retrospective. *J. Raman Spectrosc.* **2005**, *36*, 485−496.

(11) Li, K.; Hogan, N. J.; Kale, M. J.; Halas, N. J.; Nordlander, P.; Christopher, P. Balancing near-Field Enhancement, Absorption, and Scattering for Effective Antenna-Reactor Plasmonic Photocatalysis. *Nano Lett.* **2017**, *17*, 3710−3717.

(12) Robatjazi, H.; Zhao, H. Q.; Swearer, D. F.; Hogan, N. J.; Zhou, L. N.; Alabastri, A.; McClain, M. J.; Nordlander, P.; Halas, N. J. Plasmon-Induced Selective Carbon Dioxide Conversion on Earth-Abundant Aluminum-Cuprous Oxide Antenna-Reactor Nanoparticles. *Nat. Commun.* **2017**, *8*, 27.

(13) Mukherjee, S.; Libisch, F.; Large, N.; Neumann, O.; Brown, L. V.; Cheng, J.; Lassiter, J. B.; Carter, E. A.; Nordlander, P.; Halas, N. J. Hot Electrons Do the Impossible: Plasmon-Induced Dissociation of H_2 on Au. *Nano Lett.* **2013**, *13*, 240−247.

(14) Lee, J.; Mubeen, S.; Ji, X. L.; Stucky, G. D.; Moskovits, M. Plasmonic Photoanodes for Solar Water Splitting with Visible Light. *Nano Lett.* **2012**, *12*, 5014−5019.

(15) Christopher, P.; Xin, H. L.; Linic, S. Visible-Light-Enhanced Catalytic Oxidation Reactions on Plasmonic Silver Nanostructures. *Nat. Chem.* **2011**, *3*, 467−472.

(16) Christopher, P.; Xin, H. L.; Marimuthu, A.; Linic, S. Singular Characteristics and Unique Chemical Bond Activation Mechanisms of Photocatalytic Reactions on Plasmonic Nanostructures. *Nat. Mater.* **2012**, *11*, 1044−1050.

(17) Kumari, G.; Zhang, X. Q.; Devasia, D.; Heo, J.; Jain, P. K. Watching Visible Light-Driven CO_2 Reduction on a Plasmonic Nanoparticle Catalyst. *ACS Nano* **2018**, *12*, 8330−8340.

(18) Yu, S. J.; Wilson, A. J.; Heo, J.; Jain, P. K. Plasmonic Control of Multi-Electron Transfer and C-C Coupling in Visible-Light-Driven CO_2 Reduction on Au Nanoparticles. *Nano Lett.* **2018**, *18*, 2189−2194.

(19) Huang, Y. F.; Zhu, H. P.; Liu, G. K.; Wu, D. Y.; Ren, B.; Tian, Z. Q. When the Signal Is Not from the Original Molecule to Be Detected: Chemical Transformation of Para-Aminothiophenol on Ag During the Sers Measurement. *J. Am. Chem. Soc.* **2010**, *132*, 9244−9246.

(20) Boerigter, C.; Aslam, U.; Linic, S. Mechanism of Charge Transfer from Plasmonic Nanostructures to Chemically Attached Materials. *ACS Nano* **2016**, *10*, 6108−6115.

(21) Boerigter, C.; Campana, R.; Morabito, M.; Linic, S. Evidence and Implications of Direct Charge Excitation as the Dominant Mechanism in Plasmon-Mediated Photocatalysis. *Nat. Commun.* **2016**, *7*, 10545.

(22) Wu, K.; Chen, J.; McBride, J. R.; Lian, T. Efficient Hot-Electron Transfer by a Plasmon-Induced Interfacial Charge-Transfer Transition. *Science* **2015**, *349*, 632−635.

(23) Wang, F.; Li, C. H.; Chen, H. J.; Jiang, R. B.; Sun, L. D.; Li, Q.; Wang, J. F.; Yu, J. C.; Yan, C. H. Plasmonic Harvesting of Light Energy for Suzuki Coupling Reactions. *J. Am. Chem. Soc.* **2013**, *135*, 5588−5601.

(24) Li, X. Q.; Zhang, X.; Everitt, H. O.; Liu, J. Light-Induced Thermal Gradients in Ruthenium Catalysts Significantly Enhance Ammonia Production. *Nano Lett.* **2019**, *19*, 1706−1711.

(25) Zhou, L. A.; Swearer, D. F.; Zhang, C.; Robatjazi, H.; Zhao, H. Q.; Henderson, L.; Dong, L. L.; Christopher, P.; Carter, E. A.; Nordlander, P.; Halas, N. J. Quantifying Hot Carrier and Thermal Contributions in Plasmonic Photocatalysis. *Science* **2018**, *362*, 69−72.

(26) Zhang, X.; Li, X. Q.; Reish, M. E.; Zhang, D.; Su, N. Q.; Gutierrez, Y.; Moreno, F.; Yang, W. T.; Everitt, H. O.; Liu, J. Plasmon-Enhanced Catalysis: Distinguishing Thermal and Nonthermal Effects. *Nano Lett.* **2018**, *18*, 1714−1723.

(27) Kazuma, E.; Kim, Y. Mechanistic Studies of Plasmon Chemistry on Metal Catalysts. *Angew. Chem., Int. Ed.* **2019**, *58*, 4800−4808.

(28) van Schrojenstein Lantman, E. M.; Deckert-Gaudig, T.; Mank, A. J. G.; Deckert, V.; Weckhuysen, B. M. Catalytic Processes Monitored at the Nanoscale with Tip-Enhanced Raman Spectroscopy. *Nat. Nanotechnol.* **2012**, *7*, 583−586.

(29) Dong, B.; Fang, Y. R.; Chen, X. W.; Xu, H. X.; Sun, M. T. Substrate-, Wavelength-, and Time-Dependent Plasmon-Assisted Surface Catalysis Reaction of 4-Nitrobenzenethiol Dimerizing to P,P ′-Dimercaptoazobenzene on Au, Ag, and Cu Films. *Langmuir* **2011**, *27*, 10677−10682.

(30) Sun, M. T.; Xu, H. X. A Novel Application of Plasmonics: Plasmon-Driven Surface-Catalyzed Reactions. *Small* **2012**, *8*, 2777−2786.

(31) Kang, L. L.; Xu, P.; Zhang, B.; Tsai, H. H.; Han, X. J.; Wang, H. L. Laser Wavelength- and Power-Dependent Plasmon-Driven Chemical Reactions Monitored Using Single Particle Surface Enhanced Raman Spectroscopy. *Chem. Commun.* **2013**, *49*, 3389−3391.

(32) Kang, L. L.; Han, X. J.; Chu, J. Y.; Xiong, J.; He, X.; Wang, H. L.; Xu, P. In Situ Surface-Enhanced Raman Spectroscopy Study of Plasmon-Driven Catalytic Reactions of 4-Nitrothiophenol under a Controlled Atmosphere. *ChemCatChem* **2015**, *7*, 1004−1010.

(33) Xie, W.; Schlucker, S. Hot Electron-Induced Reduction of Small Molecules on Photorecycling Metal Surfaces. *Nat. Commun.* **2015**, *6*, 7570.

(34) Keller, E. L.; Frontiera, R. R. Ultrafast Nanoscale Raman Thermometry Proves Heating Is Not a Primary Mechanism for Plasmon-Driven Photocatalysis. *ACS Nano* **2018**, *12*, 5848−5855.

(35) Golubev, A. A.; Khlebtsov, B. N.; Rodriguez, R. D.; Chen, Y.; Zahn, D. R. T. Plasmonic Heating Plays a Dominant Role in the Plasmon-Induced Photocatalytic Reduction of 4-Nitrobenzenethiol. *J. Phys. Chem. C* **2018**, *122*, 5657−5663.

(36) Sarhan, R. M.; Koopman, W.; Pudell, J.; Stete, F.; Rossle, M.; Herzog, M.; Schmitt, C. N. Z.; Liebig, F.; Koetz, J.; Bargheer, M. Scaling up Nanoplasmon Catalysis: The Role of Heat Dissipation. *J. Phys. Chem. C* **2019**, *123*, 9352−9357.

(37) Sarhan, R. M.; Koopman, W.; Schuetz, R.; Schmid, T.; Liebig, F.; Koetz, J.; Bargheer, M. The Importance of Plasmonic Heating for the Plasmon-Driven Photodimerization of 4-Nitrothiophenol. *Sci. Rep.* **2019**, *9*, 3060.

(38) Choi, H. K.; Lee, K. S.; Shin, H. H.; Kim, Z. H. Identification of the First Elementary Step in the Photocatalytic Reduction of Nitrobenzenethiols on a Metallic Surface. *J. Phys. Chem. Lett.* **2016**, *7*, 4099−4104.

(39) Nelson, D. A.; Schultz, Z. D. Influence of Optically Rectified Electric Fields on the Plasmonic Photocatalysis of 4-Nitrothiophenol and 4-Aminothiophenol to 4,4-Dimercaptoazobenzene. *J. Phys. Chem. C* **2018**, *122*, 8581−8588.

(40) Takeyasu, N.; Kagawa, R.; Sakata, K.; Kaneta, T. Laser Power Threshold of Chemical Transformation on Highly Uniform Plasmonic and Catalytic Nanosurface. *J. Phys. Chem. C* **2016**, *120*, 12163−12169.

DOI: 10.1021/acs.jpcc.9b08181
J. Phys. Chem. C 2019, 123, 26695−26704

(41) Brooks, J. L.; Frontiera, R. R. Competition between Reaction and Degradation Pathways in Plasmon-Driven Photochemistry. *J. Phys. Chem. C* **2016**, *120*, 20869−20876.

(42) Zhao, L. B.; Zhang, M.; Huang, Y. F.; Williams, C. T.; Wu, D. Y.; Ren, B.; Tian, Z. Q. Theoretical Study of Plasmon-Enhanced Surface Catalytic Coupling Reactions of Aromatic Amines and Nitro Compounds. *J. Phys. Chem. Lett.* **2014**, *5*, 1259−1266.

(43) Malynych, S.; Luzinov, I.; Chumanov, G. Poly(Vinyl Pyridine) as a Universal Surface Modifier for Immobilization of Nanoparticles. *J. Phys. Chem. B* **2002**, *106*, 1280−1285.

(44) Wang, H.; Halas, N. J. Mesoscopic Au "Meatball" Particles. *Adv. Mater.* **2008**, *20*, 820−825.

(45) Zhang, Q. F.; Large, N.; Nordlander, P.; Wang, H. Porous Au Nanoparticles with Tunable Plasmon Resonances and Intense Field Enhancements for Single-Particle SERS. *J. Phys. Chem. Lett.* **2014**, *5*, 370−374.

(46) Wang, H.; Musier-Forsyth, K.; Falk, C.; Barbara, P. F. Single-Molecule Spectroscopic Study of Dynamic Nanoscale DNA Bending Behavior of HIV-1 Nucleocapsid Protein. *J. Phys. Chem. B* **2013**, *117*, 4183−4196.

(47) Xia, X. H.; Zeng, J.; Oetjen, L. K.; Li, Q. G.; Xia, Y. N. Quantitative Analysis of the Role Played by Poly(Vinylpyrrolidone) in Seed-Mediated Growth of Ag Nanocrystals. *J. Am. Chem. Soc.* **2012**, *134*, 1793−1801.

(48) Zhang, Q.; Wang, H. Mechanistic Insights on Plasmon-Driven Photocatalytic Oxidative Coupling of Thiophenol Derivatives: Evidence for Steady-State Photoactivated Oxygen. *J. Phys. Chem. C* **2018**, *122*, 5686−5697.

(49) Zheng, T. T.; Zhang, Q. F.; Feng, S.; Zhu, J. J.; Wang, Q.; Wang, H. Robust Nonenzymatic Hybrid Nanoelectrocatalysts for Signal Amplification toward Ultrasensitive Electrochemical Cytosensing. *J. Am. Chem. Soc.* **2014**, *136*, 2288−2291.

(50) Halas, N. J.; Lal, S.; Chang, W. S.; Link, S.; Nordlander, P. Plasmons in Strongly Coupled Metallic Nanostructures. *Chem. Rev.* **2011**, *111*, 3913−3961.

(51) Zhang, Q. F.; Zhou, Y. D.; Villarreal, E.; Lin, Y.; Zou, S. L.; Wang, H. Faceted Gold Nanorods: Nanocuboids, Convex Nanocuboids, and Concave Nanocuboids. *Nano Lett.* **2015**, *15*, 4161−4169.

(52) Huang, Y. F.; Wu, D. Y.; Zhu, H. P.; Zhao, L. B.; Liu, G. K.; Ren, B.; Tian, Z. Q. Surface-Enhanced Raman Spectroscopic Study of P-Aminothiophenol. *Phys. Chem. Chem. Phys.* **2012**, *14*, 8485−8497.

(53) Huang, Y. F.; Zhang, M.; Zhao, L. B.; Feng, J. M.; Wu, D. Y.; Ren, B.; Tian, Z. Q. Activation of Oxygen on Gold and Silver Nanoparticles Assisted by Surface Plasmon Resonances. *Angew. Chem., Int. Ed.* **2014**, *53*, 2353−2357.

(54) Sun, J. J.; Su, H. S.; Yue, H. L.; Huang, S. C.; Huang, T. X.; Hu, S.; Sartin, M. M.; Cheng, J.; Ren, B. Role of Adsorption Orientation in Surface Plasmon-Driven Coupling Reactions Studied by Tip-Enhanced Raman Spectroscopy. *J. Phys. Chem. Lett.* **2019**, *10*, 2306−2312.

(55) Aggarwal, R. L.; Farrar, L. W.; Saikin, S. K. Increase of SERS Signal Upon Heating or Exposure to a High-Intensity Laser Field: Benzenethiol on an AgFON Substrate. *J. Phys. Chem. C* **2012**, *116*, 16656−16659.

(56) Moskovits, M. Surface-Enhanced Spectroscopy. *Rev. Mod. Phys.* **1985**, *57*, 783−826.

(57) Wei, W.; Li, S.; Qin, L.; Xue, C.; Millstone, J. E.; Xu, X.; Schatz, G. C.; Mirkin, C. A. Surface Plasmon-Mediated Energy Transfer in Heterogap Au−Ag Nanowires. *Nano Lett.* **2008**, *8*, 3446−3449.

DOI: 10.1021/acs.jpcc.9b08181
J. Phys. Chem. C 2019, 123, 26695−26704